

Quantum Monte Carlo study on speckle variation due to photorelaxation of ferroelectric clusters in paraelectric barium titanate

Kai Ji,^{1,*} Kazumichi Namikawa,² Hang Zheng,³ and Keiichiro Nasu¹

¹ *Solid State Theory Division, Institute of Materials Structure Science, KEK, Graduate University for Advanced Studies, and CREST JST, Oho 1-1, Tsukuba, Ibaraki 305-0801, Japan*

² *Department of Physics, Tokyo Gakugei University, Nukuikita 4-1-1, Koganei, Tokyo 184-8501, Japan*

³ *Department of Physics, Shanghai Jiao Tong University, Shanghai 200030, China*

(Dated: November 9, 2018)

Time-dependent speckle pattern of paraelectric barium titanate observed in a soft x-ray laser pump-probe measurement is theoretically investigated as a correlated optical response to the pump and probe pulses. The scattering probability is calculated based on a model with coupled soft x-ray photon and ferroelectric phonon mode. It is found that the speckle variation is related with the relaxation dynamics of ferroelectric clusters created by the pump pulse. Additionally, critical slowing down of cluster relaxation arises on decreasing temperature towards the paraelectric-ferroelectric transition temperature. Relation between critical slowing down, local dipole fluctuation and crystal structure are revealed by quantum Monte Carlo simulation.

PACS numbers: 78.47.-p, 61.20.Lc, 63.70.+h, 77.80.-e

I. INTRODUCTION

Speckle is the random granular pattern produced when a coherent light is scattered off a rough surface. It carries information of the specimen surface, for the intensity and contrast of the speckle image vary with the roughness of surface being illuminated.¹ Numerous approaches have been devised to identify surface profiles by either the speckle contrast or the speckle correlation method.² Recent application of pulsed soft x-ray laser has improved the temporal and spatial resolution to a scale of picosecond and nanometer. By this means, dynamics of surface polarization clusters of barium titanate (BaTiO_3) across the Curie temperature (T_c) has been observed,^{3,4} which paves a new way to study the paraelectric-ferroelectric phase transition.

As a prototype of the ferroelectric perovskite compounds, BaTiO_3 undergoes a transition from paraelectric cubic to ferroelectric tetragonal phase at $T_c=395$ K. Below T_c , two kinds of ferroelectric domain are developed with mutually perpendicular polarization. Structural phase transition and domain induced surface corrugation have been observed via atomic force microscopy,⁵ scanning probe microscopy,⁶ neutron scattering,⁷ and polarizing optical microscopy.⁸ In addition to the extensive application of BaTiO_3 in technology due to its high dielectric constant and switchable spontaneous polarization,⁹ there is also an enduring interest in understanding the mechanism of paraelectric-ferroelectric phase transition. It is generally considered that the transition is a classic displacive soft-mode type driven by the anharmonic lattice dynamics.^{10,11} However, recent studies have also suggested an order-disorder instability which coexists with the displacive transition.^{12,13} Therefore, direct observation on creation and evolution of ferroelectric cluster around T_c is of crucial importance for clarifying the na-

ture of phase transition. Since the above-mentioned conventional time-average-based measurements cannot be adapted to the detection on ultrafast transient status of dipole clusters, diffraction speckle pattern of BaTiO_3 crystal measured by the picosecond soft x-ray laser has turned out to be an efficient way for this purpose.

Very recently, Namikawa *et al.*¹⁴ study the polarization clusters in BaTiO_3 at above T_c by the plasma-based x-ray laser speckle measurement in combination with the technique of pump probe spectroscopy. In this experiment, two consecutive soft x-ray laser pulses with wavelength of 160 Å and an adjustable time difference are generated coherently by the Michelson type beam splitter. After the photo excitation by the pump pulse, ferroelectric clusters of nano scale are created in the paraelectric BaTiO_3 and tends to be smeared out gradually on the way back to the equilibrium paraelectric state. This relaxation of cluster thus can be reflected in the variation of speckle intensity of the probe pulse as a function of its delay time from the first pulse. It has been found that the intensity of speckle pattern decays as the delay time increases. Moreover, the decay rate also decreases upon approaching T_c , indicating a critical slowing down of the cluster relaxation time. Hence, by measuring the correlation between two soft x-ray laser pulses, the real time relaxation dynamics of polarization clusters in BaTiO_3 is clearly represented. In comparison with other time-resolved spectroscopic study on BaTiO_3 , for example the photon correlation spectroscopy with visible laser beam,¹⁵ Namikawa's experiment employs pulsed soft x-ray laser as the light source. For this sake, the size of photo-created ferroelectric cluster is reduced down to a few nanometers, and the cluster relaxation time is at a scale of picosecond. This measurement, thus, offers a new insight into the ultrafast quantum dynamics of domain structure.

In this work, we examine the above-mentioned novel

behaviors of ferroelectric cluster observed by Namikawa from a theoretical point of view, aiming to provide a basis for understanding the critical nature of BaTiO₃. Theoretically, the dynamics of a system can be adequately described by the linear response theory, *i.e.*, to express the dynamic quantities in terms of time correlation functions of the corresponding dynamic operators. In general, the path integral quantum Monte Carlo method is computationally feasible to handle the quantum many body problems, for it allows the system to be treated without making any approximation. However, simulation on real time dynamics with Monte Carlo method is still an open problem in computational physics because of the formidable numerical cost of path summation which grows exponentially with the propagation time. The common approach to circumvent this problem is to perform imaginary time path integration followed by analytic continuation, and to compute the real time dynamic quantities using Fourier transformation. In the present study, the real time correlation functions and real time dependence of speckle pattern are investigated by this scheme. Our quantum Monte Carlo simulation demonstrates that the relaxation dynamics of photo-created nano clusters plays an essential role in determining the delay time dependence of speckle variation. Furthermore, it is found that the critical slowing down of photorelaxation is related to the local dipole fluctuation, which arises near T_c and stabilizes the photo-created ferroelectric cluster.

The remaining of the present paper is organized as follows. In Sec. II, the model Hamiltonian and theoretical treatment are elaborated. In Sec. III, our numerical results on speckle correlation and critical slowing down are discussed in details. In Sec. IV, a summary with conclusion is presented finally.

II. THEORETICAL MODEL AND METHODS

A. Model Hamiltonian

The theoretical interpretations for structural phase transition and domain wall dynamics have been well established in the framework of Krumhansl-Schrieffer model (also known as ϕ^4 model).^{16,17,18,19} In this model, the particles are subject to anharmonic on-site potentials and harmonic inter-site couplings. The on-site potential is represented as a polynomial form of the order parameter such as polarization, displacement, or elasticity, which displays a substantial change around T_c . Since the ϕ^4 model is only limited to second-order transitions, in the present work we invoke a modified Krumhansl-Schrieffer model (also called ϕ^6 model)^{20,21} to study the first-order ferroelectric phase transition of BaTiO₃. In this scenario, the Hamiltonian of BaTiO₃ crystal ($\equiv H_f$) is written as (here we let $\hbar = 1$),

$$H_f = -\frac{\omega_0}{2} \sum_l \frac{\partial^2}{\partial Q_l^2} + U_0 + U_i, \quad (1)$$

$$U_0 = \frac{\omega_0}{2} \sum_l \left(Q_l^2 - c_4 Q_l^4 + \frac{c_6}{3} Q_l^6 \right), \quad (2)$$

$$U_i = -\frac{\omega_0 d_2}{2} \sum_{\langle l, l' \rangle} Q_l Q_{l'}, \quad (3)$$

where, U_0 and U_i are the on-site potential and inter-site correlation, respectively. Q_l is the coordinate operator for the electric dipole moment due to a shift of titanium ions against oxygen ions, *i.e.*, the T_{1u} transverse optical phonon mode. ω_0 is the dipole oscillatory frequency, l labels the site, and $\langle l, l' \rangle$ in Eq. (3) enumerates the nearest neighboring pairs.

In order to describe the optical response of BaTiO₃ due to x-ray scattering, we design a theoretical model to incorporate the radiation field and a weak interplay between radiation and crystal. The total Hamiltonian reads,

$$H = H_p + H_f + H_{pf}, \quad (4)$$

where

$$H_p = \sum_k \Omega_k a_k^\dagger a_k, \quad \Omega_k = c|k|, \quad (5)$$

is the Hamiltonian of polarized light field. a_k^\dagger (a_k) is the creation (annihilation) operator of a photon with a wave number k and an energy Ω_k . c is the light velocity in vacuum. In Namikawa's experiment, the wave length of x-ray is 160 Å, thus the photon energy is about 80 eV. Denoting the odd parity of T_{1u} mode, the photon-phonon scattering is of a bi-linear Raman type,

$$H_{pf} = \frac{V}{N} \sum_{q, q', k} a_{k+\frac{q}{2}}^\dagger a_{k-\frac{q}{2}} Q_{q'-\frac{q}{2}} Q_{-q'-\frac{q}{2}}, \quad (6)$$

where V is the photon-phonon coupling strength, Q_q ($\equiv N^{-1/2} \sum_l e^{-iql} Q_l$) the Fourier component of Q_l with a wave number q . Without losing generality, here we use a simple cubic lattice, and the total number of lattice site is N .

B. Optical response to pump and probe photons

Since there are two photons involved in the scattering, the photon-phonon scattering probability can be written as,

$$P(t) = \sum_{k_1, k_1'} \langle \langle a_{k_0}(0) a_{k_1}^\dagger(\Delta) a_{k_0}(t) a_{k_1'}^\dagger(\Delta+t) \times a_{k_1'}(\Delta+t) a_{k_0}^\dagger(t) a_{k_1}(\Delta) a_{k_0}^\dagger(0) \rangle \rangle, \quad (7)$$

where

$$\langle \langle \dots \rangle \rangle = \text{Tr}(e^{-\beta H} \dots) / (e^{-\beta H}), \quad (8)$$

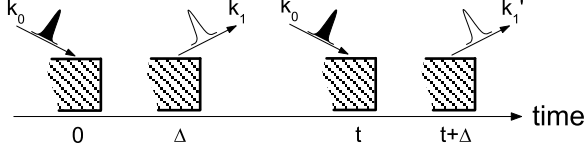


FIG. 1: Pulse sequence in an x-ray laser speckle experiment. The pump and probe pulses of k_0 creates and detects ferroelectric clusters in the sample of paraelectric BaTiO₃, respectively, and generate new x-ray fields in the direction k_1 and k'_1 after a short time interval Δ .

means the expectation, β ($\equiv 1/k_B T$) is the inverse temperature, and the time dependent operators are defined in the Heisenberg representation,

$$O(t) = e^{itH} O e^{-itH}. \quad (9)$$

Here, t denotes the time difference between two incident laser pulses as manifested in Fig. 1, and k_0 the wave number of incoming photon. After a small time interval Δ , the photon is scattered out of the crystal. k_1 and k'_1 are the wave numbers of the first and second outgoing photons, respectively.

Treating H_{pf} as a perturbation, we separate Hamiltonian of Eq. (4) as,

$$H = H_0 + H_{pf}, \quad (10)$$

where

$$H_0 = H_p + H_f, \quad (11)$$

is treated as the unperturbed Hamiltonian. By expanding the time evolution operator in Eq. (9) with respect to H_{pf} ,

$$e^{-itH} \rightarrow e^{-itH_0} \left[1 - i \int_0^t dt_1 \hat{H}_{pf}(t_1) + \dots \right], \quad (12)$$

we find that the lowest order terms which directly depend on t are of fourth order,

$$\begin{aligned} P(t) \rightarrow & \int_0^\Delta dt_1 \int_0^\Delta dt_2 \int_0^\Delta dt'_1 \int_0^\Delta dt'_2 \sum_{k_1, k'_1} \\ & \langle \langle a_{k_0} \hat{H}_{pf}(t'_1) e^{i\Delta H_0} a_{k_1}^\dagger e^{i(t-\Delta)H_f} a_{k_0} \hat{H}_{pf}(t'_2) \\ & \times e^{i\Delta H_0} a_{k'_1}^\dagger a_{k'_1} e^{-i\Delta H_0} \hat{H}_{pf}(t_2) a_{k_0}^\dagger e^{-i(t-\Delta)H_f} \\ & \times a_{k_1} e^{-i\Delta H_0} \hat{H}_{pf}(t_1) a_{k_0}^\dagger \rangle \rangle, \end{aligned} \quad (13)$$

where the operators with carets are defined in the interaction representation,

$$\hat{O}(t) = e^{itH_0} O e^{-itH_0}. \quad (14)$$

Fig. 2 represents a diagram analysis for this phonon-coupled scattering process, where photons (phonons) are depicted by the wavy (dashed) lines, and the upper (lower) horizontal time lines are corresponding to the bra (ket) vectors.²² Diagram (a) illustrates the changes of wave number and energy of photons due to the emitted or absorbed phonons. This is noting but the Stokes and anti-Stokes Raman scattering. Whereas, diagrams (b)-(e) are corresponding to the exchange, side band, rapid damping and rapid exchange effects, respectively.

Obviously, diagram (c) brings no time dependence, while diagrams (d) and (e) only contributes a rapid reduction to the time correlation of two laser pulses because of the duality in phonon interchange. In this sense, the time dependence is primarily determined by the diagrams (a) and (b). Thus, the scattering probability turns out to be,

$$\begin{aligned} P(t) = & \int_0^\Delta dt_1 \int_0^\Delta dt_2 \int_0^\Delta dt'_1 \int_0^\Delta dt'_2 \frac{2V^4}{N^4} \sum_{q, q'} \\ & \times \langle \langle a_{k_0} e^{it'_1 H_p} a_{k_0}^\dagger a_{k_0-q} e^{-i(t'_1-\Delta)H_p} a_{k_0-q}^\dagger \\ & \times a_{k_0} e^{it'_2 H_p} a_{k_0}^\dagger a_{k_0+q} e^{-i(t'_2-\Delta)H_p} a_{k_0+q}^\dagger \\ & \times a_{k_0+q} e^{i(t_2-\Delta)H_p} a_{k_0+q}^\dagger a_{k_0} e^{-it_2 H_p} a_{k_0}^\dagger \\ & \times a_{k_0-q} e^{i(t_1-\Delta)H_p} a_{k_0-q}^\dagger a_{k_0} e^{-it_1 H_p} a_{k_0}^\dagger \rangle \rangle \\ & \times \langle \langle \hat{Q}_{q'}(t'_1) \hat{Q}_{q-q'}(t'_1) \hat{Q}_{-q+q'}(t+t'_2) \\ & \times \hat{Q}_{-q'}(t+t'_2) \hat{Q}_{q'}(t+t_2) \hat{Q}_{q-q'}(t+t_2) \\ & \times \hat{Q}_{-q+q'}(t_1) \hat{Q}_{-q'}(t_1) \rangle \rangle, \end{aligned} \quad (15)$$

where the photons and phonons are decoupled, and it becomes evident that the origin of the t -dependence is nothing but the phonon (dipole) correlation.

Since the photonic part in Eq.(15) is actually time-independent, and in the case of forward x-ray scattering we have $|k_0| \approx |k_1| \approx |k'_1|$, the normalized probability can be simplified as,

$$\frac{P(t)}{P(0)} = \frac{\sum_{q, q'} |\langle \langle Q_q^2 \rangle \rangle G_{q+q'}(t)|^2}{\sum_{q, q'} |\langle \langle Q_q^2 Q_{q+q'}^2 \rangle \rangle|^2}, \quad (16)$$

where

$$G_q(t) = -i2 \langle \langle T \hat{Q}_q(t) \hat{Q}_{-q}(0) \rangle \rangle, \quad (17)$$

is the real time Green's function of phonon, and T the time ordering operator. In deriving Eq. (16), we have also made use of the fact that the light propagation time in the crystal is rather short. The Fourier component of Green's function,

$$G_q(\omega) = \int_{-\infty}^{\infty} dt G_q(t) e^{-i\omega t}, \quad (18)$$

is related to the phonon spectral function [$\equiv A_q(\omega)$] through,²³

$$G_q(\omega) = \int_{-\infty}^{\infty} \frac{d\omega'}{2\pi} \frac{A_q(\omega')}{1 - e^{-\beta\omega'}} \left(\frac{1}{\omega - \omega' + i0^+} \right)$$

$$-\frac{e^{-\beta\omega'}}{\omega - \omega' - i0^+} \Big). \quad (19)$$

The phonon spectral function describes the response of lattice to the external perturbation, yielding profound information about dynamic properties of the crystal under investigation. Once we get the spectral function, the scattering probability and correlation function can be readily derived.

C. Dynamics of crystal

A mathematically tractable approach to spectral function $A_q(\omega)$ is to introduce an imaginary time phonon Green's function, for it can be evaluated more easily than its real time counterpart. In the real space, the imaginary time Green's function is defined as,

$$G_{ll''}(\tau) \equiv -2\langle\langle T\hat{Q}_l(\tau)\hat{Q}_{l''}(0) \rangle\rangle, \quad (20)$$

where τ ($\equiv it$) is the argument for imaginary time (in this paper, we follow a convention of using Roman t for real time and Greek τ for imaginary time). The imaginary time dependence of an operator in the interaction representation is given by

$$\hat{O}(\tau) = e^{\tau H_0} O e^{-\tau H_0}. \quad (21)$$

Under the weak coupling approximation, and by using the Suzuki-Trotter identity, the Green's function can be rewritten into a path integral form (here we assume $\tau > 0$),²⁴

$$G_{ll''}(\tau) = \int \mathcal{D}x e^{-\beta[\Phi_f(x) - \Phi_f]} [-2x_l(\tau)x_{l''}(0)], \quad (22)$$

where x_l is the eigenvalue of Q_l ,

$$Q_l|x_l\rangle = x_l|x_l\rangle, \quad (23)$$

$\Phi_f(x)$ is the path-dependent phonon free energy

$$e^{-\beta\Phi_f(x)} = e^{-\int_0^\beta d\tau \Omega_f[x(\tau)]}, \quad (24)$$

with

$$\begin{aligned} \Omega_f = \sum_l \left[\frac{1}{2\omega_0} \left(\frac{\partial x_l}{\partial \tau} \right)^2 + \frac{1}{2}\omega_0 x_l^2 - \frac{1}{2}\omega_0 c_4 x_l^4 \right. \\ \left. + \frac{1}{6}\omega_0 c_6 x_l^6 \right] - \frac{1}{2}\omega_0 d_2 \sum_{\langle l, l' \rangle} x_l x_{l'}, \end{aligned} \quad (25)$$

and Φ_f is the total phonon free energy,

$$e^{-\beta\Phi_f} = \int \mathcal{D}x e^{-\beta\Phi_f(x)}. \quad (26)$$

In the path integral notation, the internal energy of crystal E_f ($\equiv \langle\langle H_f \rangle\rangle$) is represented as

$$\begin{aligned} E_f = \int \mathcal{D}x e^{-\beta[\Phi_f(x) - \Phi_f]} \left[\omega_0 \sum_l \left(x_l^2 - \frac{3}{2}c_4 x_l^4 \right. \right. \\ \left. \left. + \frac{2}{3}c_6 x_l^6 \right) - \omega_0 d_2 \sum_{\langle l, l' \rangle} x_l x_{l'} \right], \end{aligned} \quad (27)$$

from which the heat capacity can be derived as

$$C_f^V = \left(\frac{\partial E_f}{\partial T} \right)_V. \quad (28)$$

The Green's function of momentum space is given by,

$$G_q(\tau) = \frac{1}{N} \sum_{l, l''} e^{iq(l-l'')} G_{ll''}(\tau), \quad (29)$$

which is connected with the phonon spectral function $A_q(\omega)$ through²⁵

$$G_q(\tau) = - \int_0^\infty \frac{d\omega}{2\pi} \frac{\cosh \left[\left(\frac{1}{2}\beta - \tau \right) \omega \right]}{\sinh \left(\frac{1}{2}\beta\omega \right)} A_q(\omega). \quad (30)$$

Solving this integral equation is a notoriously ill-posed numerical problem because of the highly singular nature of the kernel. In order to analytically continue the imaginary time data into real frequency information, specialized methods are developed, such as maximum entropy method²⁶ and least squares fitting method.²⁷ In present work, we adopt the iterative fitting approach,²⁴ for it can give a rapid and stable convergence of the spectrum without using any prior knowledge or artificial parameter. Since the phonon spectral function does not yield a specific sum rule like the case of electron, here we introduce an auxiliary spectral function $\tilde{A}_q(\omega)$ which is defined by

$$\tilde{A}_q(\omega) \equiv - \frac{\coth \left(\frac{1}{2}\beta\omega \right)}{G_q(\beta)} A_q(\omega). \quad (31)$$

Substituting $\tilde{A}_q(\omega)$ into Eq. (30), we get

$$G_q(\tau) = \int_0^\infty \frac{d\omega}{2\pi} \frac{\cosh \left[\left(\frac{1}{2}\beta - \tau \right) \omega \right]}{\cosh \left(\frac{1}{2}\beta\omega \right)} G_q(\beta) \tilde{A}_q(\omega). \quad (32)$$

It can be easily shown that this auxiliary spectral function satisfies a sum rule,

$$\int_0^\infty \frac{d\omega}{2\pi} \tilde{A}_q(\omega) = 1, \quad (33)$$

which allow us to solve the integral equation of Eq. (32) by the iterative fitting approach. Once $\tilde{A}_q(\omega)$ is reproduced, the phonon spectral function $A_q(\omega)$ can be obtained from Eq. (31).

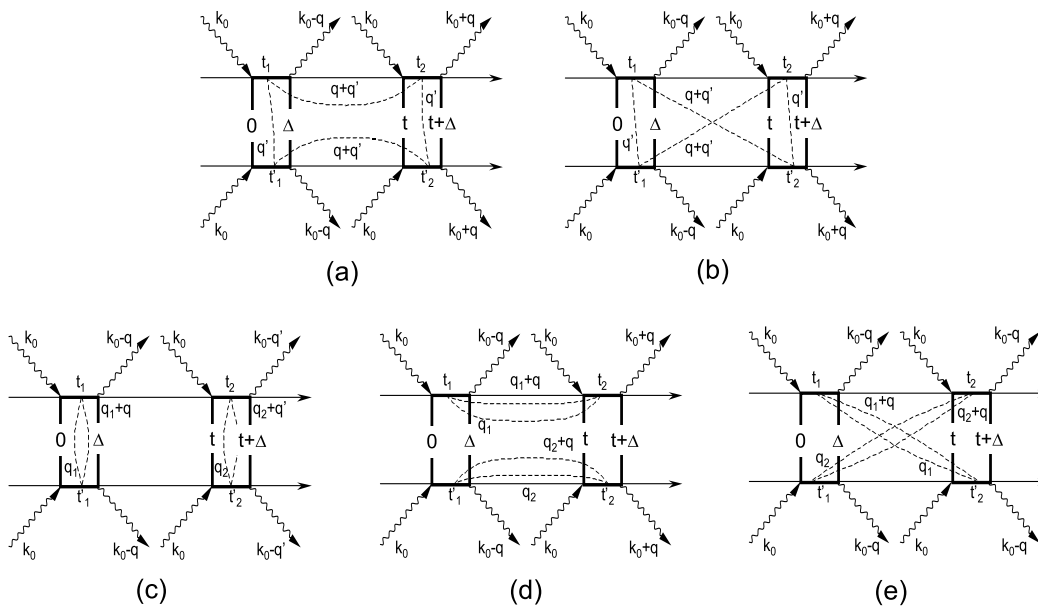


FIG. 2: Double-sided Feynman diagrams for scattering process of photon with electric dipole moment (phonon). The photons and phonons are denoted by the wavy and dashed lines, respectively. In each diagram, the upper and lower horizontal time lines represent the bra and ket vectors, respectively.

III. NUMERICAL RESULTS AND DISCUSSION

A. Optical responses

Based on the path integral formalisms, the imaginary time Green's function can be readily calculated via a standard quantum Monte Carlo simulation.²⁴ Our numerical calculation is performed on a $10 \times 10 \times 10$ cubic lattice with a periodic boundary condition. The imaginary time is discretized into 10-20 infinitesimal slices. As already noticed for the analytic continuation,²⁸ if the imaginary time Green's function is noisy, the uncertainty involved in the inverse transform might be very large, and the spectral function cannot be determined uniquely. In order to obtain accurate data from quantum Monte Carlo simulation, a hybrid algorithm²⁴ has been implemented in our calculation. Besides, we pick out each Monte Carlo sample after 100-200 steps to reduce the correlation between adjacent configurations. The Monte Carlo data are divided into 5-10 sets, from which the 95% confidence interval is estimated through 10,000 resampled set averages by the percentile bootstrap method. We found that about 1,000,000 Monte Carlo configurations are sufficient to get well converged spectral functions and real time dynamic quantities.

In the numerical calculation, the phonon frequency ω_0 is assumed to be 20 meV,²⁹ the inter-site coupling constant d_2 is fixed at a value of 0.032, whereas c_4 and c_6 are selected to make the on-site U_0 a symmetric triple-well potential. As shown in Fig. 3, this triple-well structure is featured by five potential extrema located at x_a , $\pm x_b$

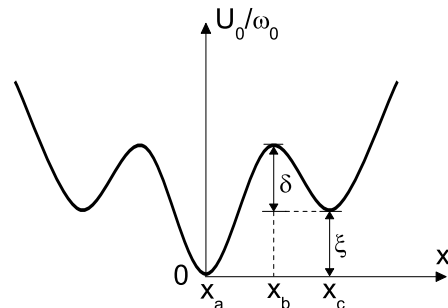


FIG. 3: On-site potential U_0 for the modified Krumhansl-Schrieffer model in the unit of ω_0 . The coordinates of potential extrema are denoted by x_a , x_b , and x_c . δ and ξ are two parameters adopted to characterize this potential.

and $\pm x_c$, where

$$x_a = 0, \quad (34)$$

$$x_b = \sqrt{\frac{c_4 - \sqrt{c_4^2 - c_6}}{c_6}}, \quad (35)$$

$$x_c = \sqrt{\frac{c_4 + \sqrt{c_4^2 - c_6}}{c_6}}. \quad (36)$$

In Figs. 4 and 5, we show the optical responses of crystal, where $c_4 = 2.0132 \times 10^{-2}$ and $c_6 = 3.2595 \times 10^{-4}$ are used. Fig. 4 presents the phonon spectral functions in the paraelectric phase at different temperatures: (a) $T = 1.001T_c$, (b) $T = 1.012T_c$, (c) $T = 1.059T_c$ and (d)

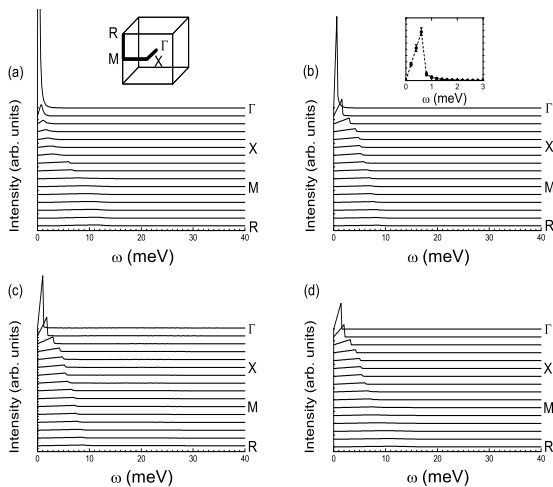


FIG. 4: Phonon spectral function along the line ΓXMR of Brillouin zone in the paraelectric phase at various temperatures: (a) $1.001T_c$, (b) $1.012T_c$, (c) $1.059T_c$, and (d) $1.176T_c$, where $T_c=386$ K. The inset of panel (a) shows the Brillouin zone with high symmetry lines. The inset of panel (b) represents the spectrum at Γ point for $T=1.012T_c$ is plotted with 95% confidence interval illustrated by the error bars. Since the spectra are symmetric with respect to the origin $\omega=0$, here we only show the positive part of them. In Fig. 4, when the temperature decreases towards T_c , as already well-known for the displacive type phase transition, the energy of phonon peak is gradually softened. In addition, a so-called central peak, corresponding to the low energy excitation of ferroelectric cluster, appears at the Γ point. The collective excitation represented by this sharp resonant peak is nothing but the photo-created ferroelectric cluster. On decreasing temperature, spontaneous polarization is developed locally as a dipole fluctuation in the paraelectric phase. This fluctuation can stabilize the photo-created ferroelectric cluster, leading to a dramatically enhanced peak intensity near T_c .

$T=1.176T_c$, where $T_c=386$ K. In each panel, the spectra are arranged with wave vectors along the ΓXMR direction of Brillouin zone [see in the inset of panel (a)], and ω refers to energy. In the inset of panel (b), the spectrum at Γ point for $T=1.012T_c$ is plotted with 95% confidence interval illustrated by the error bars. Since the spectra are symmetric with respect to the origin $\omega=0$, here we only show the positive part of them. In Fig. 4, when the temperature decreases towards T_c , as already well-known for the displacive type phase transition, the energy of phonon peak is gradually softened. In addition, a so-called central peak, corresponding to the low energy excitation of ferroelectric cluster, appears at the Γ point. The collective excitation represented by this sharp resonant peak is nothing but the photo-created ferroelectric cluster. On decreasing temperature, spontaneous polarization is developed locally as a dipole fluctuation in the paraelectric phase. This fluctuation can stabilize the photo-created ferroelectric cluster, leading to a dramatically enhanced peak intensity near T_c .

The appearance of sharp peak at Γ point nearby T_c signifies a long life-time of the photo-created ferroelectric clusters after irradiation. Thus, near T_c , they are more likely to be probed by subsequent laser pulse, resulting in a high intensity of speckle pattern. Keeping this in mind, we move on to the results of scattering probability. In Fig. 5, we show the variation of normalized probability $P(t)/P(0)$ as a function of t (time interval between the pump and probe photons). Temperatures for these curves correspond to those in the panels (a)-(d) of Fig. 4, respectively. In this figure, $P(t)/P(0)$ declines exponentially, showing that the speckle correlation decreases with

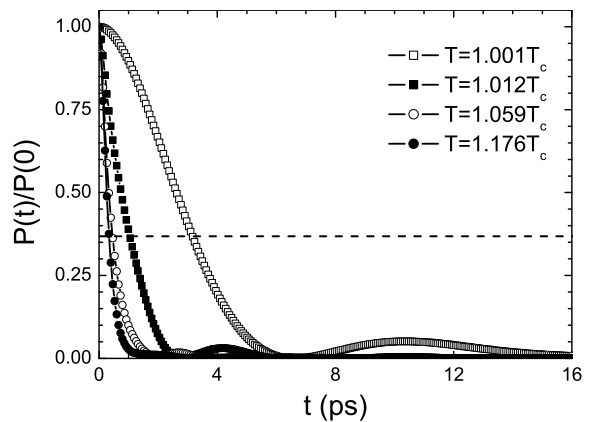


FIG. 5: Normalized speckle scattering probability as a function of time for paraelectric $BaTiO_3$, at various temperatures. Horizontal dashed line denotes $P(t) = P(0)/e$.

t increases as a result of the photorelaxation of ferroelectric cluster. When t is long enough, the crystal returns to the equilibrium paraelectric state. In addition, as shown in the figure, the relaxation rate bears a temperature dependence. On approaching T_c , the duration for return is prolonged, indicative of a critical slowing down of the relaxation. This is because with the decrease of temperature, the fluctuation of local polarization is enhanced, and a long range correlation between dipole moments is to be established as well, making the relaxation of photo-created clusters slower and slower.

B. Critical slowing down of photorelaxation

In order to quantitatively depict the critical slowing down, we introduce a relaxation time t_r to estimate the time scale of relaxation, which is the time for $P(t)$ to be reduced by a factor of e from $P(0)$. In Fig. 5, $P(t)=P(0)/e$ is plotted by a horizontal dashed line. Correspondingly, t_r is the abscissa of the intersection point of relaxation curve and this dashed line. In Fig. 6, the relaxation time for various local potential U_0 is presented at $T > T_c$. Here we adopt two legible parameters, δ and ξ , to describe the potential wells and barriers for U_0 (see Fig. 3), which are defined by

$$\delta \equiv [U_0(x_b) - U_0(x_c)]/\omega_0, \quad (37)$$

$$\xi \equiv U_0(x_c)/\omega_0. \quad (38)$$

Provided δ and ξ , c_4 and c_6 can be derived in terms of Eqs. (35)-(38). The values of c_4 and c_6 for the calculation of Fig. 6 are listed in Table I, where we set $\xi=3.061$ and change δ from 4.239 to 4.639. The leftmost point on each curve denotes the t_r at just above T_c , which is a temperature determined from the singular point of C_f^Y according to Eq. (28).

As revealed by the NMR experiment,¹² the

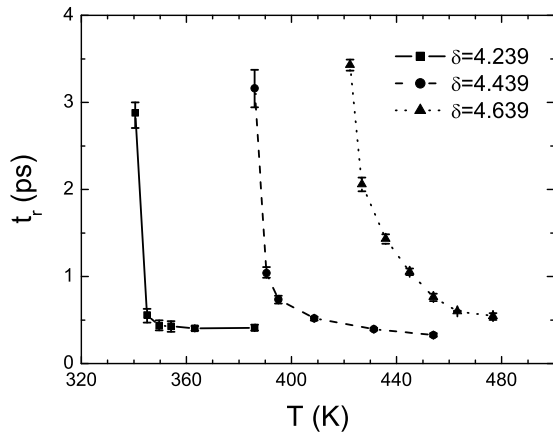


FIG. 6: Temperature dependence of relaxation time t_r for various δ when $T > T_c$, where ξ is fixed at 4.439. Error bars show the 95% confidence interval.

TABLE I: Parameters adopted for calculation of Fig. 6.

c_4	c_6	δ	ξ	T_c (K)
2.0696×10^{-2}	3.4521×10^{-4}	4.239	3.061	340
2.0132×10^{-2}	3.2593×10^{-4}	4.439	3.061	386
1.9596×10^{-2}	3.0814×10^{-4}	4.639	3.061	422

paraelectric-ferroelectric phase transition of BaTiO_3 has both displacive and order-disorder components in its mechanism. Short range dipole fluctuation arises in the paraelectric phase near T_c as a precursor of the order-disorder transition, and condenses into long range ferroelectric ordering below T_c . Thus, in the present study, the relaxation of photo-created cluster is also subject to the dynamics of this dipole fluctuation and yields a temperature dependence. As illustrated by the three curves in Fig. 6, if a ferroelectric cluster is created at a temperature close to T_c , relaxation of this cluster is slow because of a rather strong dipole fluctuation, which holds the cluster in the metastable ferroelectric state from going back to the paraelectric one. Away from T_c , t_r decreases considerably for the dipole fluctuation is highly suppressed. This behavior is nothing but the critical slowing down of photorelaxation.

In Fig. 6, it can also be seen that with the increase of δ , T_c moves to the high temperature side so as to overcome a higher potential barrier between the ferroelectric and paraelectric phases. Furthermore, the evolution of t_r becomes gentle as well, implying a gradual weakening of dipole fluctuation at high temperature region.

In Fig. 7, we show the temperature dependence of t_r for different ξ when $T > T_c$, where δ is fixed at 4.439. The values of parameters for this calculation are given in Table II. When ξ changes from 3.261 to 2.861, as shown in Fig. 7, T_c gradually increases. This is because with the decrease of ξ , the ferroelectric state at x_c (refer to Fig. 3)

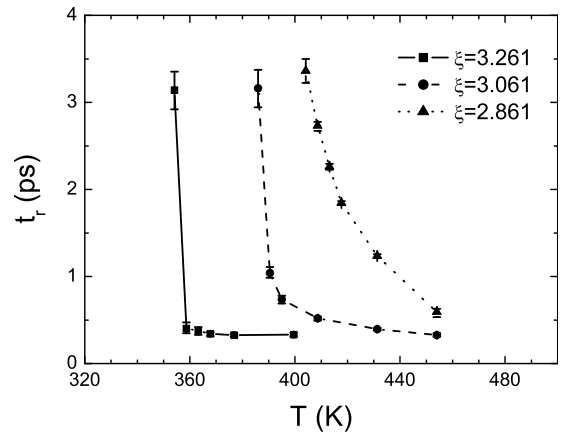


FIG. 7: Temperature dependence of relaxation time t_r for various ξ when $T > T_c$, where δ is fixed at 3.061. Error bars show the 95% confidence interval.

TABLE II: Parameters adopted for calculation of Fig. 7.

c_4	c_6	δ	ξ	T_c (K)
1.9626×10^{-2}	3.1070×10^{-4}	4.439	3.261	354
2.0132×10^{-2}	3.2593×10^{-4}	4.439	3.061	386
2.0663×10^{-2}	3.4223×10^{-4}	4.439	2.861	404

becomes more stable and can survive even larger thermal fluctuation. In a manner analogous to Fig. 6, the evolution of t_r also displays a sharp decline at low temperature, and becomes more and more smooth as temperature increases.

In Fig. 8, we plot the temperature dependence of t_r for different barrier heights, *i.e.*, $\delta + \xi$ varies from 7.0 to 8.0, while the ratio δ/ξ is fixed at 1.5. Parameters for

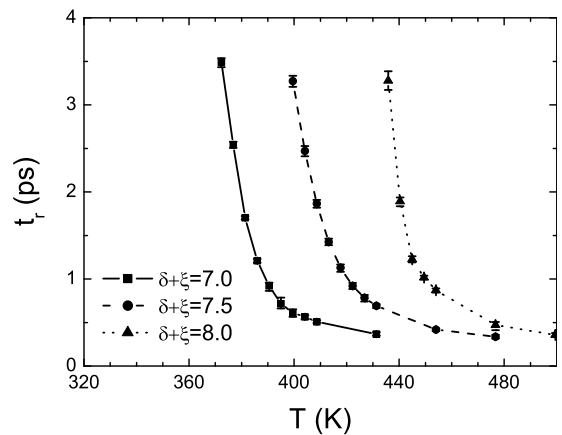


FIG. 8: Temperature dependence of relaxation time t_r for various barrier height $\delta + \xi$ when $T > T_c$, where $\delta/\xi=1.5$ is assumed. Error bars show the 95% confidence interval.

TABLE III: Parameters adopted for calculation of Fig. 8.

c_4	c_6	δ	ξ	$\delta + \xi$	T_c (K)
2.1557×10^{-2}	3.7309×10^{-4}	4.200	2.800	7.000	372
2.0122×10^{-2}	3.2505×10^{-4}	4.500	3.000	7.500	400
1.8860×10^{-2}	2.8557×10^{-4}	4.800	3.200	8.000	436

this calculation are provided in Table III. As already discussed with Figs. 6 and 7, larger δ tends to increase T_c , but higher ξ applies an opposite effect on T_c . Combining these two effects, in Fig. 8, one finds that T_c increases if both δ and ξ are enhanced, indicating that in this case, the change of δ plays a more significant role. Meanwhile, in contrast to Figs. 6 and 7, all the three curves in Fig. 8 present smooth crossovers on decreasing temperature towards T_c , signifying that dipole fluctuation can be promoted by lowering ξ even the temperature is decreased.

In Namikawa's experiment, the wavelength of soft x-ray laser is 160 Å, hence the photo-created cluster is of nano scale. However, it should be noted that relaxation of nano-sized cluster is beyond our present quantum Monte Carlo simulation because of the size limitation of our model. This is the primary reason why the experimentally measured relaxation time can reach about 30 picoseconds, being several times longer than our calculated results. In spite of the difference, our calculation has well clarified the critical dynamics of BaTiO₃ and the origin of speckle variation.

IV. SUMMARY

We carry out a theoretical investigation to clarify the dynamic property of photo-created ferroelectric cluster observed in the paraelectric BaTiO₃ as a real time correlation of speckle pattern between two soft x-ray laser pulses. The density matrix is calculated by a perturbative expansion up to the fourth order terms, so as to characterize the time dependence of scattering probability. The cluster-associated phonon softening as well as central peak effects are well reproduced in the phonon spectral function via a quantum Monte Carlo simulation. We show that the time dependence of speckle pattern is determined by the relaxation dynamics of photo-created ferroelectric cluster, which is manifested as a central peak in the phonon spectral function. The photorelaxation of ferroelectric cluster is featured by a critical slowing down on decreasing the temperature. Near the T_c , cluster excitation is stabilized by the strong dipole fluctuation, correspondingly the relaxation becomes slow. While, at higher temperature, dipole fluctuation is suppressed, ending up with a quicker relaxation of cluster. Our simulation also illustrates that the critical slowing down and dipole fluctuation are subject to the chemical environment of crystal.

V. ACKNOWLEDGMENTS

This work is supported by the Next Generation Supercomputer Project, Nanoscience Program, MEXT, Japan.

-
- * Electronic address: jikai@post.kek.jp
- ¹ M. May, J. Phys. E **10** 849 (1977).
 - ² J. W. Goodman, *Speckle Phenomena in Optics: Theory and Applications* (Roberts and Company, Greenwood Village, 2007).
 - ³ R. Z. Tai, K. Namikawa, M. Kishimoto, M. Tanaka, K. Sukeyama, N. Hasegawa, T. Kawachi, M. Kado, P. Lu, K. Nagashima, H. Daido, H. Maruyama, A. Sawada, M. Ando, and Y. Kato, Phys. Rev. Lett. **89**, 257602 (2002).
 - ⁴ R. Z. Tai, K. Namikawa, A. Sawada, M. Kishimoto, M. Tanaka, P. Lu, K. Nagashima, H. Maruyama, and M. Ando, Phys. Rev. Lett. **93**, 087601 (2004).
 - ⁵ S.-I. Hamazaki, F. Shimizu, S. Kojima, and M. Takashige, J. Phys. Soc. Jpn. **64** 3660 (1995).
 - ⁶ G. K. H. Pang and K. Z. Baba-Kishi, J. Phys. D **31** 2846 (1998).
 - ⁷ Y. Yamada, G. Shirane, and A. Linz, Phys. Rev. **177** 848 (1969).
 - ⁸ W. L. Mulvihill, K. Uchino, Z. Li and W. Cao, Phil. Mag. B **74** 25 (1996).
 - ⁹ D. L. Polla and L. F. Francis, Annu. Rev. Mater. Sci. **28** 563 (1998).
 - ¹⁰ J. Harada, J. D. Axe, and G. Shirane, Phys. Rev. B **4** 155 (1971).
 - ¹¹ R. Migoni, D. Bauer, and H. Bilz, Phys. Rev. Lett. **37** 1155 (1976).
 - ¹² B. Zalar, V. V. Laguta, and R. Blinc Phys. Rev. Lett. **90** 037601 (2003).
 - ¹³ G. Völkel and K. A. Müller, Phys. Rev. B **76** 094105 (2007).
 - ¹⁴ K. Namikawa, unpublished.
 - ¹⁵ R. Yan, Z. Guo, R. Tai, H. Xu, X. Zhao, D. Lin, X. Li, and H. Luo, Appl. Phys. Lett. **93**, 192908 (2008).
 - ¹⁶ J. A. Krumhansl and J. R. Schrieffer, Phys. Rev. B **11**, 3535 (1975).
 - ¹⁷ S. Aubry, J. Chem. Phys. **62** 3217 (1975).
 - ¹⁸ T. Schneider and E. Stoll, Phys. Rev. B **17**, 1302 (1978).
 - ¹⁹ V. V. Savkin, A. N. Rubtsov, and T. Janssen, Phys. Rev. B **65** 214103 (2002).
 - ²⁰ J. R. Morris and R. J. Gooding, Phys. Rev. Lett. **65**, 1769 (1990).
 - ²¹ A. Khare, A. Saxena, J. Math. Phys. **49**, 063301 (2008).
 - ²² K. Nasu, J. Phys. Soc. Jpn. **63**, 2416 (1994).
 - ²³ S. Doniach and E. H. Sondheimer, *Green's Function for Solid State Physicists*, (Benjamin, London, 1974), Appendix 2.
 - ²⁴ K. Ji, H. Zheng, and K. Nasu, Phys. Rev. B **70**, 085110 (2004).
 - ²⁵ J. Bonča and J. E. Gubernatis, Phys. Rev. B **53**, 6504 (1996).
 - ²⁶ Skilling and R. K. Bryan, Mon. Not. R. Astron. Soc. **211**, 111 (1984).
 - ²⁷ M. Yamazaki, N. Tomita, and K. Nasu, J. Phys. Soc. Jpn. **72**, 611 (2003).

- ²⁸ J. E. Gubernatis, M. Jarrell, R. N. Silver, and D. S. Sivia
Phys. Rev. B **44**, 6011 (1991).
- ²⁹ W. Zhong, R. D. King-Smith, and D. Vanderbilt, Phys.
Rev. Lett. **72**, 3618 (1994).